7-10-2013

Unveiling the Roles of Binder in the Mechanical Integrity of Electrodes for Lithium-Ion Batteries

Jianchao Chen
University of South Carolina - Columbia, chenji@mailbox.sc.edu

Jianyong Liu

Yue Qi

Tao Sun

Xiaodong Li
University of South Carolina - Columbia, lixiao@cec.sc.edu

Publication Info

Published in *Journal of The Electrochemical Society*, Volume 160, Issue 9, 2013, pages A1502-A1509.

Publisher's Version: http://dx.doi.orgg/10.1149/2.088309jes
Chen, J., Liu, J., Qi, Y., Sun, T., & Li, X. (2013). Unveiling the Roles of Binder in the Mechanical Integrity of Electrodes for Lithium-Ion Batteries. Journal of The Electrochemical Society, 160 (9), A1502-A1509. http://dx.doi.orgg/10.1149/2.088309jes

Journal of The Electrochemical Society, **160** (9) A1502-A1509 (2013)
0013-4651/2013/160(9)/A1502/8/$31.00 © The Electrochemical Society

Unveiling the Roles of Binder in the Mechanical Integrity of Electrodes for Lithium-Ion Batteries

Jianchao Chen,[a,b] Jianyong Liu,[c] Yue Qi,[d,*,z] Tao Sun,[b] and Xiaodong Li[a,z]

[a]*Department of Mechanical Engineering, University of South Carolina, Columbia, South Carolina 29201, USA*
[b]*Center for Precision Engineering, Harbin Institute of Technology, Harbin 150001, China*
[c]*General Motors (China) Investment Corporation, Shanghai 201206, China*
[d]*General Motors Research and Development Center, Warren, Michigan 48090, USA*

In lithium-ion secondary batteries research, binders have received the least attention, although the electrochemical performance of Li-ion batteries such as specific capacity and cycle life cannot be achieved if the adhesion strengths between electrode particles and between electrode films and current collectors are insufficient to endure charge-discharge cycling. In this paper, the roles of binders in the mechanical integrity of electrodes for lithium-ion batteries were studied by coupled microscratch and digital image correlation (DIC) techniques. A microscratch based composite model was developed to decouple the carbon particle/particle cohesion strength from the electrode-film/copper-current-collector adhesion strength. The dependences of microscratch coefficient of friction and the critical delamination load on the PVDF binder content suggest that the strength of different interfaces is ranked as follows: Cu/PVDF < carbon-particle/PVDF < PVDF/PVDF. The particle/particle cohesion strength increases while electrode-film/current-collector adhesion strength decreases with increasing PVDF binder content (up to 20% of binder). The electrolyte soaking-and-drying process leads to an increase in particle/particle cohesion but a decrease in electrode-film/copper-current-collector adhesion. Finally, the methodology developed here can provide new guidelines for binder selection and electrode design and lay a constitutive foundation for modeling the mechanical properties and performance of the porous electrodes in lithium-ion batteries.
 [DOI: 10.1149/2.088309jes]

Manuscript submitted May 13, 2013; revised manuscript received June 25, 2013. Published July 10, 2013.

In the automotive industry, transformational changes in battery technologies are critically needed to move from hybrid electric vehicles (HEV) to plug-in HEV (PHEV), and all-electric vehicles (EV). Lithium-ion secondary batteries (Li-ion batteries) have become the main power source for portable electronics because of their high gravimetric and volumetric capacities.[1,2] However for PHEV and EV applications, much higher energy/power density and longer shelf/cycle life are essential. To achieve such performance, intense research has been focused on the development of the following four cell materials: positive and negative electrode active materials (AM), separators, and electrolytes.[1–4] In contrast, less attention has been paid to binders, the electrochemically inactive materials, which hold electrode particles together and further bond the AM particle-based electrode film to its substrate – the current collector. It is as important as other four materials in Li-ion batteries, since the electrochemical performance such as specific capacity and cycle life cannot be achieved if the electrode-particle/electrode-particle and/or electrode-film/current-collector adhesion strengths are insufficient to endure charge-discharge cycling.

It has been shown that improved adhesion leads to better retention of discharge capacity during cycling, especially when electrode materials exhibit faster or/and larger volume expansion. Recently Liu et al.[5] reported that the long-range electronic conductivity in a composite electrode is almost exclusively ascribed to the bond strength of the binder (mixed with conductive carbon black). A higher binder loading resulted in the formation of a more cohesive conductive carbon particle network and consequently better capacity retention, especially in the greater C rate regime. Recently, Lee et. al.[6] found that a strong correlation exists between particle/binder adhesion strength and the retention rate of discharge capacity. Binder properties can be particularly important for high capacity AMs, since higher capacity is associated with greater volume expansion during lithiation. For example, for a Si-Sn system (which exhibits huge volume expansion up to 250% upon alloying with lithium), even though the amorphous Si-Sn particles do not fracture during expansion and contraction, capacity loss is ascribed to the loss of the electrical contact between the particles due to the poor mechanical, more specifically adhesion, properties of the binder.[7,8]

In addition to affecting battery cell performance, binder also plays an important role in battery cell manufacture. External stress, which is inevitable in cell manufacturing processes such as calendaring and winding, may unbind the AM particles and/or delaminate the electrode film from its current collector. The detached AM particles, particularly electronically conductive particles such as graphite, can penetrate the cell separator during winding, leading to cell internal shortening.[9]

Most of these studies were performed with the commercially available binder, polyvinylidene fluoride (PVDF), which is widely used in Li-ion batteries because of its electrochemical stability at the high voltage range. In recent years, new binder development includes (1) seeking new electronically conductive binders with high elasticity in order to accommodate the large volume change of AMs during insertion and extraction of lithium-ions,[7,10–17] (2) replacing the costly, environmentally unfriendly, and volatile organic solvent used in the manufacturing of electrode,[18–20] and (3) increasing the adhesion strength between the binder and other components of electrode (AMs and conductive materials in general).[5,21–26] However, the development of binders is hindered by the lack of standard tests of binder adhesion properties and a fundamental understanding of adhesion mechanism.

A standard method is thus required to evaluate the basic properties of binders – maintaining the mechanical integrity of AM particle/particle and electrode-film/current-collector. These properties are not only important for the pristine electrodes, but also for the electrodes in solutions, as the polar electrolyte solvent can have a significant impact on the mechanical properties and electrical conductivity of electrode. It has been demonstrated that electrical conductivity is decreased when the electrode is submerged in the electrolyte solvent, because swelling of PVDF results in an increase in spacing between conductive carbon particles.[5] Such performance loss was shown to be reversible after the solvent dried out in a fresh electrode.[27] Yoo et. al.[28] found that the adhesion of the dry electrode to its collector is higher than that of swollen ("wet") electrode. During battery cycling, electrolyte may dry out and the mechanical consequences of the dry-out after battery aging are not completely known. It is of great interest to compare the binder properties in the pristine sample with the sample treated by solvent soaking and drying.

Various non-standard testing methods have been applied to probe binder properties. To evaluate the robustness of electrode, Zabhib et. al.[29] developed a loop stiffness tester. In their experiments, the composite electrode coating along with the current collector was rolled into a cylinder shape (with the electrode coating facing out); then compressed until the electrode fractured. Dahn et. al.[27] developed a coupled stress-strain and resistivity tester to probe simultaneously the mechanical and electrical properties of an electrode along with the

*Electrochemical Society Active Member.
[z]E-mail: yue.qi@gm.com; lixiao@cec.sc.edu

binder immersed in the liquid solvent. Peel test[6,26] and scratch test[28] have been used to measure the adhesion of an electrode film to its substrate and to study the influence of suspension (used in negative electrode fabrication) on the performance of the electrode. However, these macroscopic testing methods were not able to distinguish the particle/binder/particle cohesion and electrode-film/binder/current-collector adhesion. For example, using macro-scratch tests, Yoo et. al.[28] evaluated the adhesion between the electrode-film and current-collector by measuring the critical load at which the electrode-film was completely removed. They found that the adhesion of the electrode-film with the current collector was increased by either promoting chemical bonds at the particle/binder interface or increasing the strength of PVDF by increasing its crystallinity. In their macro-scratch test,[28] the scratch tip was on the order of millimeters, much larger than typical 5∼10 μm electrode particles. It is thus impossible to deconvolute the particle/particle cohesion strength from electrode-film/current-collector adhesion strength by using such a macro-scratch test, although the method has been used to semi-quantitatively evaluate the adhesion of a coating to its substrate.[30,31]

To fundamentally understand the roles of the binder in maintaining the mechanical integrity of electrodes for lithium-ion batteries, we have conducted a systematic study of the particle/particle cohesion and electrode-film/current-collector adhesion provided by the binder phase. For this purpose, we used a scratch tip with a tip radius an order of magnitude smaller than the AM particles (8∼16 μm, mesocarbon microbead (MCMB) particles for this study). Both the diamond scratch tip and MCMB particles can be treated as rigid bodies with respect to the soft binder. Thus the scratch tangential force mainly comes from the plowing force that separates the bonded particles rather than that fractures the particles.[32] Therefore, the coefficient of friction (COF) obtained during scratching before the scratch tip encounters the substrate should be a measure of particle/particle cohesion strength. Similar to the macro-scratch test, the critical delamination load also provides a semi-quantitative measure of electrode-film/current-collector adhesion strength. In order to further investigate the load transfer ability at the particle/binder/particle interface, we accompanied the micro-scratch tests with digital image correlation (DIC) analysis, which has been widely used to measure local microscale deformation. The load transfer mechanism at the particle/polymer interface in polymer composite materials was recently revealed by mapping local micro-scale strain fields using the DIC technique.[33,34]

Typically, the binder content is 1–3% for consuming electronics application, and is nearly doubled for EV and HEV application for longer cycle life requirements. In order to reveal the role of binder including the property of binder itself, in this paper, we investigated the electrode composites with binder content ranging from 5% to 100% and designed a group of micro-scratch and DIC experiments to elucidate the binder bonding mechanisms at both the particle/binder/particle interface (referred as the cohesion between particles or at the particle/particle interface) and the electrode-film/binder/current-collector interface (referred as the adhesion of electrode-film to current-collector or at the electrode-film/current-collector interface). By analyzing the scratch and DIC results as a function of binder content, we decoupled the particle/particle cohesion strength from the electrode-film/current-collector adhesion strength. We found that higher particle/particle cohesion strength does not necessarily guarantee a higher electrode-film/substrate adhesion strength. On the contrary, an increase in particle/particle cohesion strength with the increasing binder content in the electrode-film results in a decrease in electrode-film/substrate adhesion. Furthermore, by comparing the pristine and the electrolyte treated samples, we found that the soaking-and-drying leads to an increase in particle/particle cohesion but a decrease in electrode-film/current-collector adhesion.

Experimental

Electrode-film preparation.— Active anode material – MCMB was purchased from Shanghai Shanshan Inc. PVDF binder was supplied by Arkema, Inc. 1-methy1-2-pyrrolidinone (NMP) was purchased from Maiqi, Inc. A given amount of PVDF binder was dissolved in NMP to obtain 4 wt% PVDF solution, which was then stored in a 85°C oven for 12 h. Uniform slurries with different MCMB/PVDF ratios were made by adding dried MCMB powders into the PVDF solution and then manually mixing them in an agate mortar for about 30 min. The slurries were then cast onto 9 μm thick copper foils using the doctor-blade method. The slurry films were dried at 85°C in a vacuum oven (Heraeus VT 6130) for 12 h. The weight fraction of PVDF binder in the electrodes (dry weight) was 5, 10, 20, 50, 80, and 100 wt%, respectively.

To prepare the soaked-dried electrodes, an area of 20 mm × 20 mm was cut from each electrode. The sample was first immersed in an electrolyte solvent mixture of ethylene carbonate (EC) and dimethyl carbonate (DMC) at the volume ratio of 1:1 for 7 h at room temperature. Both EC and DMC were acquired from Alfa Aesar. All samples were separately sealed in liquid containers filled with fresh solvent mixture. The swollen electrodes after soaking were taken out and dried in a vacuum oven at 83°C for 12 h. Here we limit our focus to the soaking and drying effects caused solely by the electrolyte solvent without adding the lithium salt, which is very sensitive to water and thus inappropriate for the mechanical tests in ambient condition.

The thicknesses of the as-prepared MCMB/PVDF electrode-films were measured by imaging the cross sections of freshly cut electrode-films using an optical microscope. For comparison, electrodes of similar film thickness were selected for mechanical testing. Micro-indentation tests were performed on both the pristine and the soaked-dried anode films using a load-depth sensing Nano UTM universal testing machine (Agilent Technologies, Inc) at a loading rate of 200 mN/min under load control mode. The indenter tip is a tungsten carbide ball of 3.17 mm in diameter. The Young's modulus of the electrode films was derived using the classic Hertz contact model by fitting the load–indentation depth curve in the elastic deformation regime. For details about micro-indentation tests, please see Refs 35 and 36. The details regarding the anode composite films, their thicknesses and Young's moduli are listed in Table I.

Table I. Compositions, thicknesses, and Young's moduli of the anode electrode films.

Name	PVDF/Total[a] (%, w/w)	MCMB/Total[a] (%, w/w)	Film Thickness (μm)	Young's Modulus (GPa)	
				Pristine	Soaked-dried
A-5-1-N	5	95	39	0.140	0.149
A-10-2-2-T	10	90	41	0.197	0.190
A-20-3	20	80	56	0.068	0.074
A-50-4	50	50	36	0.085	0.095
A-80-5	80	20	18.6	0.141	0.226
A-100-6-1	100	0	10.6	0.980	0.817

[a]Total weight of the electrode film including PVDF and MCMB.

Digital image correlation (DIC).— A custom-built computer-controlled tensile tester in conjunction with an Olympus PME3 inverted optical microscope equipped with a CCD camera was used to perform in-situ imaging and tensile testing on both the pristine and the soaked-dried electrode samples. The samples, in the form of 20 mm long strips with a width of 4 mm, were cut using a razor blade. A small V-shaped single edge notch was opened on the specimen edge to induce a stress concentration site in order to facilitate the observation of the strain development and crack propagation. The tensile stage with a left-right combination lead screw was employed to stretch the sample to minimize the movement of the imaging area, which was kept close to the central area of 400 μm × 500 μm right below notch tip for about 1 mm under various applied strains. Once the electrode sample was set and gripped in the tester, the tensile test was carried out by incremental displacement steps. The minimum strain step was $1.6\% \times 10^{-2}$. At each step the tension force was monitored and recorded, and simultaneously, the corresponding optical image of the region of interest was digitally captured in-situ by the CCD camera. The tensile tester has a load resolution of 100 mN with a capacity of 180 N. The optical images obtained before and after stretching the samples were processed using a Vic-2D 2009 DIC program package (Correlated Solutions Inc.). Two-dimensional surface displacement and strain field maps were constructed by comparing the optical images of the same area of each sample before and after deformation. For details about DIC, please see Refs 33 and 37.

Microscratch test.— The adhesion strength between the electrode-film and the copper current collector and the cohesion strength between the MCMB particles with binder were measured by scratching the film surface with a tip using a CETR Tribometer (Bruker Inc.). A conical diamond stylus having a tip radius of 1.5 μm and a cone angle of 60° was used. The scratch tip was drawn over the film surface and a 2 mm long scratch track was then made by translating the sample while linearly ramping up the normal load on the conical tip from 6 mN to 50 mN. During scratching, the tangential force F_t and normal force F_n were detected real time in-situ. The particle/particle cohesion strength was semi-qualitatively evaluated by analyzing the coefficient of friction (COF), which can be readily calculated by F_t/F_n. A schematic illustration of the scratching test, along with the scratch track and measured normal and tangential forces is given in Figure 1. The scratch track was examined by a FEI Quanta 200 environmental scanning electron microscope (E-SEM) operating at 25 kV. The minimum normal load F_n, at which the film delaminates from the copper substrate, is defined as the critical delamination load as a measure of the electrode-film/current-collector adhesion strength.

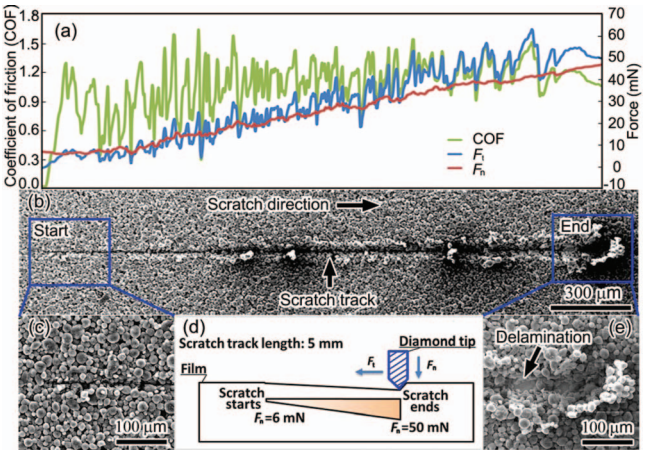

Figure 1. (a) normal force F_n, tangential force F_t, and coefficient of friction curve of sample A-5-1-N as a function of scratching distance. (b) SEM image of the scratch track of A-5-1-N. (c) and (e) SEM images of the beginning and end of the scratch track, respectively. (d) Schematic illustration of the scratching test.

Results and Discussion

Morphologies of composite electrode films with different binder contents.— Figure 2 shows the SEM images of MCMB/PVDF anode composite films with different PVDF binder contents (5%, 10%, 20%, 50%, 80%, and 100 wt%). Along with the SEM images, the insets in Figure 2 schematically illustrate the MCMB/PVDF interaction. At low PVDF contents (5% in Figure 2a and 10% in Figure 2b), the electrode-films exhibited a stack of packed spherical MCMB particles with the diameter ranging from 8 to 16 μm. The binder did not appear to coat entire particle's surface to form a shell when the binder content was less than 10%, which is in good agreement with the results obtained from other particle/binder systems.[29,38] With an increase in binder content (20% in Figure 2c and 50% in Figure 2d), the PVDF conformably formed shell layers (coatings) on MCMB particles (Figure 2c and 2d) to adhere the particles together as indicated by the dashed circle in Figure 2c. The increase of PVDF content resulted in SEM image blurring, as shown in Figure 2c and Figure 2d, due to the charging effect of the electrically non-conductive PVDF. This, in turn, validates that higher binder content produces thicker shells on the MCMB particles and increases the particle/binder interface area, as schematically illustrated in the insets in Figure 2c and Figure 2d. Further increasing PVDF content will allow us to probe the properties of PVDF experimentally. Figure 2e and Figure 2f show the SEM images of the electrode-film with 80% PVDF and the pure PVDF film, respectively. In the film with 80% PVDF, few isolated MCMB

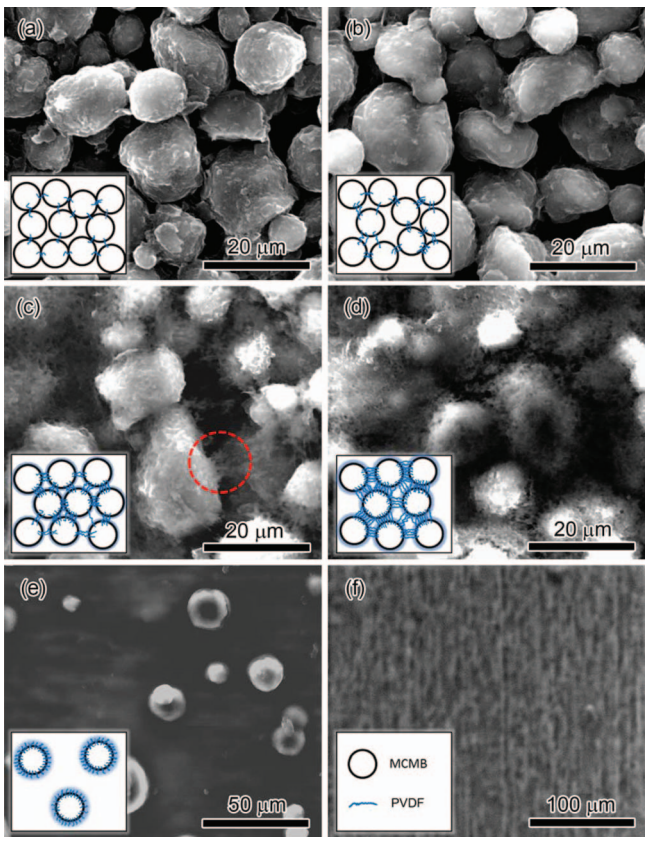

Figure 2. SEM images of pristine MCMB/PVDF composites: (a) A-5-1-N, MCMB (95%)/PVDF (5%). (b) A-10-2-2-T, MCMB (90%)/PVDF (10%). (c) A-20-3, MCMB (80%)/PVDF (20%). Polymer bridging particles as indicated by the dashed circle. (d) A-50-4, MCMB (50%)/PVDF (50%). (e) A-80-5, MCMB (20%)/PVDF (80%). (f) A-100-6-1, pure PVDF (100%). Insets are schematic graphs illustrating the binder function for the MCMB/PVDF films.

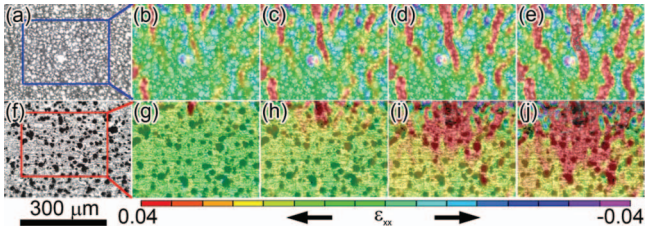

Figure 3. Optical micrographs of (a) A-10-2-2-T (10% PVDF loading, soaked-dried) and (f) A-80-5 (80% PVDF loading, soaked-dried) without applied tensile strain. (b-e) DIC strain maps of the rectangle area in (a) with different applied tensile strains: (b) 3.776; (c) 4.032; (d) 4.16; (e) 4.416%. (g-j) DIC strain maps of the rectangle area in (f) with different applied tensile strain: (g) 3.52; (h) 3.84; (i) 4.032; (j) 4.096%. Arrows under picture indicate the orientation of applied tensile strain. The positive color-coded horizontal strain ε_{xx} is parallel to the tensile direction.

particles were embedded in a binder polymer matrix. In comparison, a homogenous distribution of MCMB particles was achieved in the electrode-films with 5, 10, 20, and 50% binder loading.

Strain filed mapping of the composite electrode films with DIC.— To investigate the deformation mechanism of the composite electrode-films, especially to elucidate the role of binder in binding particles, we performed in-situ tensile tests on the composite electrode-films using a micromechanical tester in conjunction with the optical microscope. To stretch the electrode-film samples, tensile strain was gradually applied to the films along the direction denoted by the arrows in Figure 3. The optical images of the un-stretched films were used as the reference images for processing the images obtained from the stretched films with DIC. A low-binder-content film A-10-2-2-T (10% PVDF, soaked-dried) and a high binder loading film A-80-5 (80% PVDF, soaked-dried) are presented in Figure 3. All images covered an electrode area of 423 × 317 μm of electrode with a resolution of 0.331 μm. The subset (grid) used in DIC processing was 23.17 × 23.17 μm, therefore the local strain resolution was larger than the particle diameter (8∼16 μm). Figure 3a and Figure 3f show the optical images of the two un-stretched films (0% applied tensile strain). Figure 3b-3e and 3g-3j show the optical images overlapped with the corresponding local strain field maps along the tension direction at different applied overall strains. The local strain maps show clearly that the strain was not uniform in the films, but rather unevenly distributed in a wave-like manner, perpendicular to the tension direction. Thinner wave-like strain concentration bands were found in the low binder loading sample (Figure 3b-3e) whereas for the high binder loading film, fewer but wider strain concentration strips were presented (Figure 3g-3j). Note that the strain concentration bands in both film samples consist of both PVDF binder and MCMB particles, indicating strong bonding and load transferring between the PVDF binder and the MCMB particles. The strong bond was consistent with the semi-ionic and covalent bond characters of C–F bonds formed at the graphite/PVDF interface.[28] In addition to the strong bonding between the PVDF binder and the MCMB particles, the ligaments between particles (interparticle route) are also vital for load transfer across the film, which also contributes to the mechanical properties of the entire film. As discussed in Section 3.1, for the film with high binder loading, the binder between particles is expected to function as a polymer matrix to provide strong bond between particles, and thus allows load to be transferred effectively and evenly. This can be validated by the DIC results. Figure 3g-3j show that the binder phase was elongated as the applied strain was increased, which ultimately formed a wide and relatively homogeneous strain distribution, as shown in Figure 3j. In contrast, for the electrode film with low binder content, fewer ligaments were found in interparticle pores as illustrated in Figure 2b. The paucity of ligaments depressed inter-particle load transfer in the film. Namely, the deformation localized on the interparticle route may be detoured or disconnected upon external mechanical loading. Therefore, as shown in Figure 3b-3e, strain concentration spots emerged in multiple stress-vulnerable areas where ligaments were absent (load transfer route was disconnected). With further increasing of the applied strain, these strain concentration spots began to connect and form wave-shaped strips, which then widen as shown in Figure 3e.

Microscratching of the composite electrode-films.— To further study the role of binder in the electrode-film, we carried out microscratch tests on both pristine and soaked-dried electrode-film samples listed in Table I. The coefficient of friction (COF) curves as a function of normal load are illustrated in Figure 4. At the beginning of scratch,

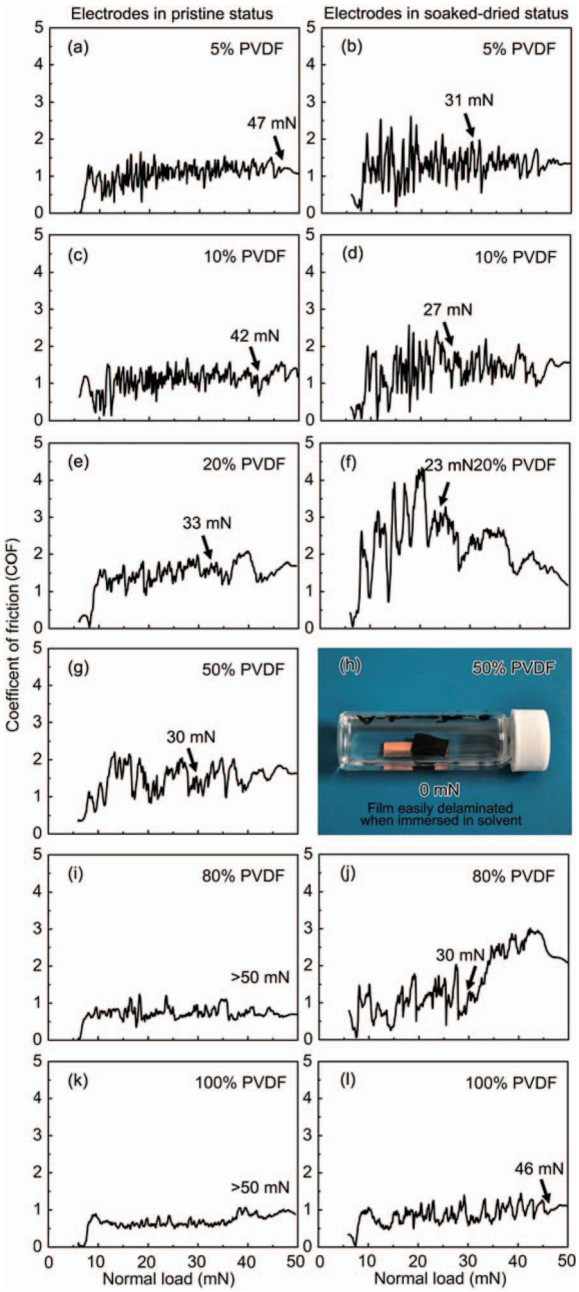

Figure 4. Coefficient of friction (COF) as a function of normal load for (a, c, e, g, i, k) pristine and (b, d, f, j, l) soaked-dried samples listed in Table I (h) Digital camera image of the soaked-dried sample A-50-5 (MCMB (50%)/PVDF (50%)).The film immediately delaminated from substrate after being soaked, the scratching test was impossible. The critical delamination load (critical load) for each film, at which the film was found to delaminate from the copper substrate from SEM images, is indicated on its COF curve.

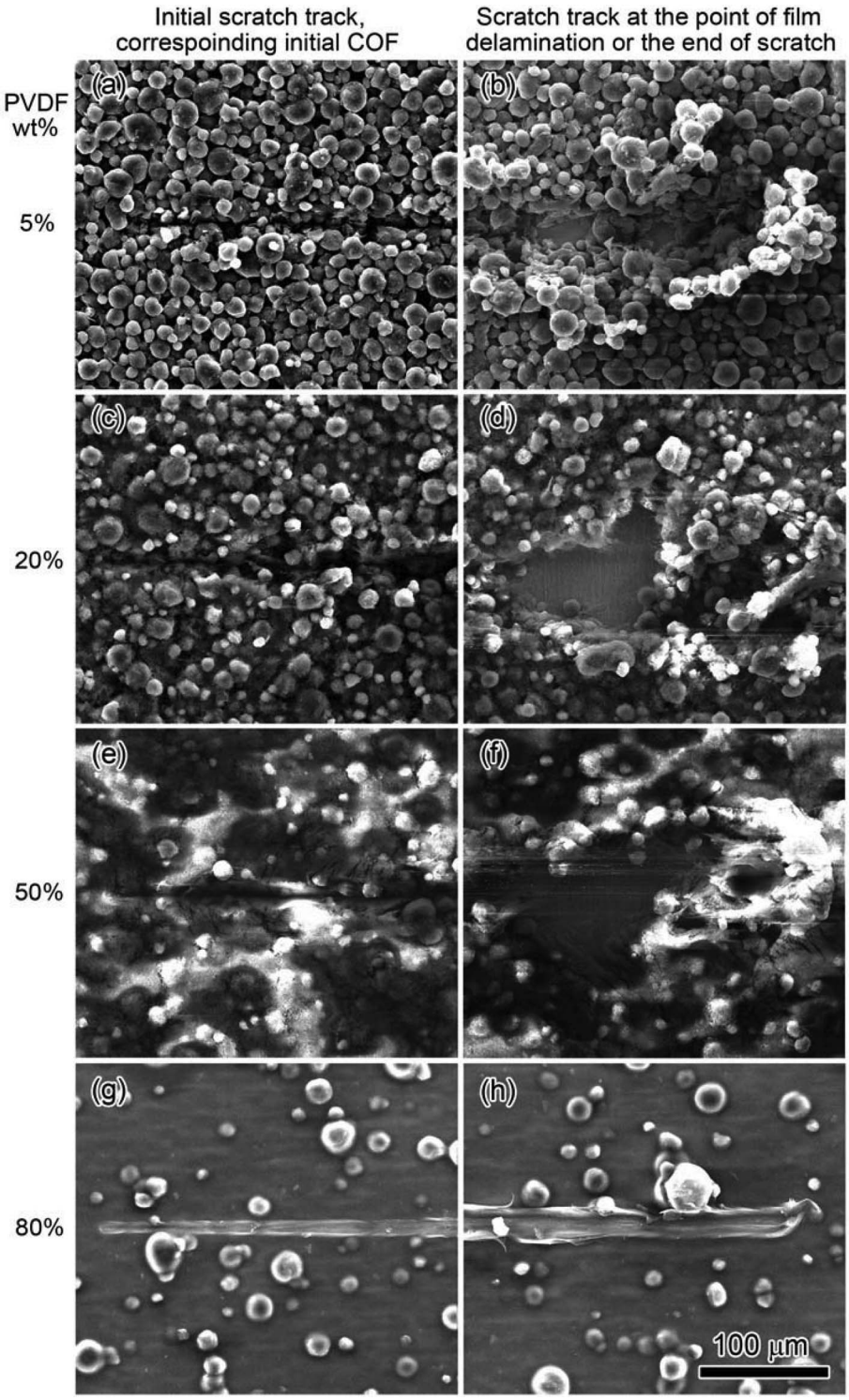

Figure 5. SEM images of the beginning and end of microscratch tracks for pristine samples with different PVDF binder contents.

the COF for all samples increased rapidly with increasing normal load because the tip started to plow and slide on the sample surface. With further increasing the normal load, the COF reached a steady state except for the three soaked-dried samples: A-20-3 (20% PVDF), A-50-4 (50% PVDF), and A-80-5 (80% PVDF), as shown in Figure 4f, 4h, and 4j. For electrode A-20-3 (soaked-dried) (Figure 4f), the COF fluctuated until a catastrophic failure at the critical load of 23 mN. The electrode film of A-50-4 (Figure 4h) delaminated from its substrate immediately after soaking and drying, and thus we assumed that its critical delamination load was zero. This suggests that soaking and drying of an electrode in electrolyte solvent can induce the electrode-film delamination. For sample A-80-5 (Figure 4j), its COF remained almost constant at the beginning and then slightly increased before the film delaminates at 30 mN. Beyond the critical delamination load, the COF increased abruptly, which was attributed to the noticeable delaminated debris piled-up around the scratch tip. The critical delamination loads for each sample were pointed out using arrows in Figure 4. The SEM images of the scratch tracks at the initial and end of micro-scratch test (or at the film delamination point) for the pristine samples with 5, 20, 50, and 80% PVDF loading are presented in Figure 5. Flat current collector regions can be seen in Figure 5b, 5d, and 5f for the samples with 5%, 20% and 50% PVDF binder

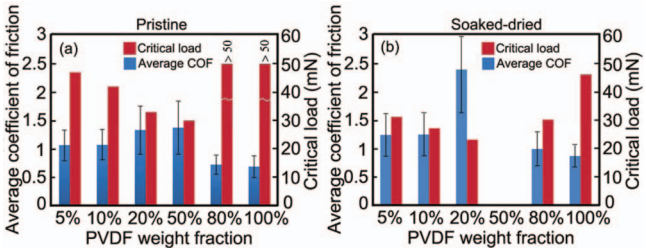

Figure 6. Comparison of the average coefficient of friction and critical load for respective (a) pristine and (b) soaked-dried samples at different binder concentration. Average COF (the blue bar) along with its deviation was calculated by averaging the friction data in the normal force range from initial load (6 mN) to the critical load. The critical loads indicated in Fig. 4 were also summarized here (the red bar).

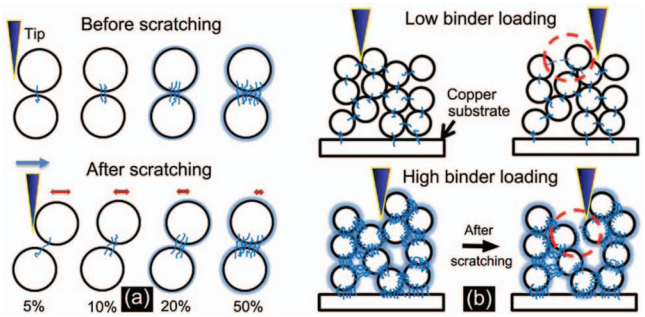

Figure 7. Schematic illustration of the scratch process in a MBMC/PVDF coated copper electrode. (a) Simplified model describing the interaction between particles in samples with different PVDF loading (5, 10, 20, and 50%). The length of red arrows indicates the displacement when particles falling apart: the longer the arrows, the larger the displacement is. (b) The crack propagation progress during scratching in composite with low and high binder loading.

content, indicating film delamination. Typically, thicker films can bear more normal load before film delaminates, however the critical delamination load of the electrode-films did not show such thickness dependence but rather show much more dependence on PVDF binder content. For the pristine samples with binder content >=80%, no delamination was observed up to 50 mN, as shown in Figure 5h (the image taken at the end of scratch track where 50 mN normal load was applied).

The micro-scratch tests provide two pieces of vital information: (1) the COF averaged from initial load (6 mN) to the critical delamination load in the micro-scratch test indicates the particle/particle cohesion strength, especially at low binder content; and (2) the critical delamination load indicates the electrode-film/current-collector adhesion strength. Figure 6a and 6b summarize the average values of COF and critical delamination load for both pristine and soaked-dried samples at different binder contents. Both values show a strong binder content dependence. The COF first increases with increasing PVDF content, peaked at 50% PVDF for pristine sample (or 20% PVDF for soaked-dried sample), then dropped with overwhelming amount of PVDF (80% and 100% PVDF). The critical normal load at which the film delaminated from the copper current collector also varied with binder content, but exhibited an opposite trend comparing to the COF. The critical delamination strength of electrode-films decreased with increasing binder content, reached a lowest value around 50% PVDF content, and then increased for samples with very high PVDF contents (80% and 100%). These dependences on PVDF content hold for both the pristine and soaked-dried samples. The sample with the highest COF exhibited the lowest critical delamination load. Comparing the pristine samples with soaked-dried samples, the COF increased but the critical delamination load decreased after the soaking-drying treatment. The results clearly show that the particle/particle cohesion and film/current-collector adhesion are two distinct quantities. The seemingly contradictory dependence on binder content can be explained by a composite model derived from the DIC and micro-scratch results.

Composite electrode model.— Figure 7 schematically illustrates the micro-scratch process in a composite model for the MBMC/PVDF coated copper electrode-film. As the micro-tip scratches through the binder phase between particles, the tangential force F_t mainly balances the plowing force rather than the sliding friction force when scratching the low-binder-content electrode-films (5, 10, 20, and 50% of PVDF content). This is evident from the SEM images of the initial scratch tracks, which show clear separation between particles, at 5% and 20% binder content (Figure 5a and 5c). Thus the COF is a measure of the particle/particle cohesion strength provided by the binder phase. As seen from the morphology of the electrode in Figure 2, the amount of ligaments between the particles increases with binder content until the binder phase wraps the entire particle. Assuming f_b is the force that is required to break up the C–F bond at the particle/binder interface the particle/particle cohesion strength provided by the binder phase scales with the number of C-F bonds formed on a unit area at particle/binder/particle interface, Σ. Thus, the COF, or the tangential force F_t is directly related to the particle/particle cohesion strength, σ_{coh}, in a simplified form as follows:[39]

$$COF \propto F_t \propto \sigma_{coh} = f_b \Sigma \quad [1]$$

Clearly, an increase in PVDF binder content gives rise to a higher Σ, therefore enhancing the particle/binder/particle cohesion strength. This is in good agreement with Lestriez and co-workers' observation[40] that the maximum calendaring pressure (in a different representation particle/particle cohesion strength) increases with the ratio of the amount of binder in the electrode-film and the surface area of the particles. The above findings are also consistent with what we proposed in section 3.2 – the low cohesion strength causes weak load transfer capability. At very high binder level (80% PVDF), particles become further apart, and the viscoelastic PVDF polymer is more scratch resistant,[41] as a result very shallow penetration depth was observed as shown in Figure 5g. We also noticed that the electrode-film modulus listed in Table I measured via micro-indentation experiment, do not vary largely for composite films, however the modulus of pure PVDF film is four times larger than the rest of the samples. Thus, the COFs of the samples containing 80% and 100% binder do not represent the particle/particle cohesion strength but represent the intrinsic scratching resistant of PVDF itself. The high scratch resistance and modulus of PVDF indicates the PVDF/PVDF interaction is stronger than carbon/PVDF interaction.

Figure 7b illustrates how a micro-tip initiates a crack for the composite electrode. To make the film delaminate from its substrate, a crack needs to initiate from the micro-indenter tip then penetrate into and propagate along the electrode film/current-collector interface. For the electrode-films with low binder content, the fracture energy is quickly dissipated by pushing particles away in the upper surface as indicated by the red dashed-circle in the low binder loading sample in Figure 7b. Therefore, it is difficult for the crack to penetrate into the electrode-film/current-collector interface. Even though the crack starts to propagate, it will be deflected in a zigzag manner between the densely packed particles in a similar fashion as shown in the DIC image Figure 3b-3e. This suggests that the slight decrease of the critical delamination load is also related to particle piling-up during microscratch test. Lower binder content leads to lower particle/particle cohesion, more piling up (as shown in Figure 5b), thus higher normal load for delamination. The extremely high critical delamination load for 80% and 100% PVDF film indicates that these films should be considered as a rigid body rather than a composite electrode model. Furthermore, as the binder content increases, the amount of ligaments at the particle/current-collector interface should have increased as well. However, it seems that the critical delamination load does not increase with the binder content, suggesting that the delamination occurs at the Cu/PVDF interface and this interface is

much weaker than the carbon/PVDF interface. Moreover, it should be noted that Table I lists only representative samples with similar thickness (expect the two samples with very high PVDF content). Scratch tests were also performed on the samples with significantly different thicknesses (not included in the paper). It turned out to be that the thicker film delaminates at a higher critical load. Based on our model, for thicker films (both low and high binder loading samples), the crack path is inevitable to be increased and the crack has more chances to be deflected, thus the fracture energy required for delamination is higher, suggesting that for films with same binder loading, the thicker film has a higher delamination strength (the adhesion between electrode and current collector).

By comparing the pristine and soaked-dried samples, we notice that the soaking-drying process leads to a slight increase in COF but a big decrease in critical delamination load, as shown in Figure 6. Especially, as shown in Figure 4h, the corresponding soaked-dried samples are more prone to delamination from the current collector. The SEM images show more smeared binder phase between particles after the soaking and drying treatment, leading to an increase in particle/particle cohesion. The electrode will be under compression during soaking and under tension during drying. This tensile stress will lead to film delamination even at a lower normal load in the micro-scratch test. Thus, it is much easier for the soaked-dried sample to delaminate from substrate comparing to the pristine samples (in Figure 5). During battery cycling, the amount of electrolyte will be reduced due to electrolyte decomposition, the dry-out of electrolyte can lead to electrode/current collector delamination if no compression is applied to the battery cell, consequently capacity fading and cell resistance increase.

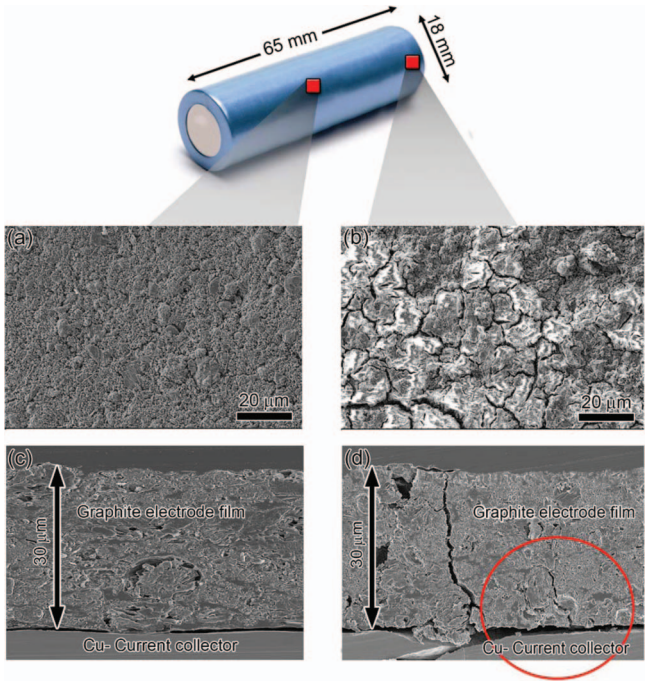

Figure 8. SEM images taken from a cycled commercial 18650 battery cell, which has lost 45% of its capacity, to illustrate the nature of heterogeneous mechanical degradation and binder failure. Image (a) and (b) show top view of the graphite electrodes taken from different locations in the cycled cell. No obvious cracks were found in (a) from the middle of the cell, but inter-particle cracks were found in (b) taken close to the end cap. (c) shows the side view of the (a) region. (d) shows the side view of the (b) region, where cracks initiated from electrode/current collector interface either penetrates the electrode to be seen in (b) or only half-way through the electrode, indicating the Cu/PVDF interaction is less than particle/binder interaction.

Implication for Li-ion battery.— The microsctrach tests provide semi-quantitative measure of both particle/particle cohesion and electrode-film/current-collector adhesion strength. Since the PVDF binder loading in Li-ion battery is typically only a few percent, we shall focus more on the results with 5% to 20% binder loading. Even 5% PVDF can provide the adhesion at the particle-to-particle interface to maintain the mechanical integrity of the composites. At this level of binder content, the particle/particle cohesion strength increases while electrode-film/substrate adhesion strength decreases with increasing PVDF binder content. Based on the composite electrode model, combining the dependences of COF and the critical delamination load on the PVDF binder content, we believe the strength at different interfaces following this order: Cu/PVDF < MCMB/PVDF < PVDF/PVDF.

This conclusion is consistent with the failure analysis performed in a commercial Li-ion battery, which exhibited large mechanical degradation. In many cases, degradation and failure in large format batteries starts locally at inhomogeneities or weak points. Figure 8 highlights the spatial inhomogeneity in the graphite anode of a commercial 18650 battery after it lost ~45% of its capacity after fast C rate cycling. The graphite anode develops inter-particle cracks damage (Figure 8b) near each end cap, and the damage contributes significantly to the substantial loss of capacity. In comparison, the central region of the electrode tape was largely smooth, homogeneous (Figure 8a) and still can be fully charged. Figure 8d further shows the side view of the graphite anode in Figure 8b. It can been seen that cracks initiated from electrode/current-collector interface either penetrate the electrode to appear as an inter-particle crack seen in Figure 8b or only half-way through the electrode, indicating the Cu/PVDF interaction is less than graphite/PVDF interaction.

Conclusions

A coherent picture of the binder's roles in the mechanical integrity of electrodes for lithium-ion batteries has been mapped out by coupled micro-scratch and digital image correlation (DIC) techniques. A micro-scratch based composite model has been developed to decouple the carbon particle/particle cohesion strength from the electrode-film/copper-current-collector adhesion strength. Both micro-scratch and DIC experiments showed that even 5% polyvinylidene fluoride (PVDF) can provide the adhesion at the particle-to-particle interface to maintain the mechanical integrity of the composite electrodes. At this level of binder content, the particle/particle cohesion strength increases while the electrode-film/substrate adhesion strength decreases with increasing PVDF binder content. The dependences of the micro-scratch coefficient of friction and the critical delamination load on the PVDF binder content suggest that the strength of different interfaces is ranked as follows: Cu/PVDF < carbon-particle/PVDF < PVDF/PVDF. The soaking-and-drying process leads to an increase in particle/particle cohesion but a decrease in electrode-film/copper-current-collector adhesion. The findings provide new guidelines for binder selection and electrode design and lay a constitutive foundation for modeling the performance of the electrodes in lithium-ion batteries.

Acknowledgments

JC acknowledges the financial support from China Scholarship Council. XL thanks the support from the U.S. National Science Foundation (CMMI-1129979). The authors also thank the University of South Carolina EM Center staff members for SEM support.

References

1. J. B. Goodenough and Y. Kim, *Chem. Mater.*, **22**, 587 (2010).
2. P. G. Bruce, B. Scrosati, and J.-M. Tarascon, *Angew. Chem. Int. Ed.*, **47**, 2930 (2008).
3. F. Cheng, J. Liang, Z. Tao, and J. Chen, *Adv. Mater.*, **23**, 1695 (2011).
4. C. Liu, F. Li, L.-P. Ma, and H.-M. Cheng, *Adv. Mater.*, **22**, E28 (2010).
5. G. Liu, H. Zheng, A. S. Simens, A. M. Minor, X. Song, and V. S. Battaglia, *J. Electrochem. Soc.*, **154**, A1129 (2007).
6. J. H. Lee, U. Paik, V. A. Hackley, and Y. M. Choi, *J. Power Sources*, **161**, 612 (2006).

7. Z. H. Chen, L. Christensen, and J. R. Dahn, *J. Electrochem. Soc.*, **150**, A1073 (2003).
8. Z. H. Chen, L. Christensen, and J. R. Dahn, *J. Appl. Polym. Sci.*, **90**, 1891 (2003).
9. X. Huang, *J. Solid State Electrochem.*, **15**, 649 (2011).
10. Z. H. Chen, L. Christensen, and J. R. Dahn, *Electrochem. Commun.*, **5**, 919 (2003).
11. G. Liu, S. Xun, N. Vukmirovic, X. Song, P. Olalde-elasco, H. Zheng, V. S. Battaglia, L. Wang, and W. Yang, *Adv. Mater.* **23**, 4679 (2011).
12. I. Kovalenko, B. Zdyrko, A. Magasinski, B. Hertzberg, Z. Milicev, R. Burtovyy, I. Luzinov, and G. Yushin, *Science*, **333**, 75 (2011).
13. F. M. Courtel, S. Niketic, D. Duguay, Y. Abu-Lebdeh, and I. J. Davidson, *J. Power Sources*, **196**, 2128 (2011).
14. J. Li, D. B. Le, P. P. Ferguson, and J. R. Dahn, *Electrochim. Acta*, **55**, 2991 (2010).
15. A. Magasinski, B. Zdyrko, I. Kovalenko, B. Hertzberg, R. Burtovyy, C. F. Huebner, T. F. Fuller, I. Luzinov, and G. Yushin, *ACS Appl. Mater. Interfaces*, **2**, 3004 (2010).
16. N. Ding, J. Xu, Y. Yao, G. Wegner, I. Lieberwirth, and C. Chen, *J. Power Sources*, **192**, 644 (2009).
17. N. S. Choi, K. H. Yew, W.-U. Choi, and S.-S. Kim, *J. Power Sources*, **177**, 590 (2008).
18. G. T. Kim, S. S. Jeong, M. Joost, E. Rocca, M. Winter, S. Passerini, and A. Balducci, *J. Power Sources*, **196**, 2187 (2011).
19. S. F. Lux, F. Schappacher, A. Balducci, S. Passerini, and M. Winter, *J. Electrochem. Soc.*, **157**, A320 (2010).
20. J. Chong, S. Xun, H. Zheng, X. Song, G. Liu, P. Ridgway, J. Q. Wang, and V. S. Battaglia, *J. Power Sources*, **196**, 7707 (2011).
21. D. Guy, B. Lestriez, R. Bouchet, V. Gaudefroy, and D. Guyomard, *Electrochem. Solid-State Lett.*, **8**, A17 (2005).
22. B. Lestrie, S. Bahri, I. Sandu, L. Roue, and D. Guyomard, *Electrochem. Commun.*, **9**, 2801 (2007).
23. B. Lestriez, *C.R. Chim.*, **13**, 1341 (2010).
24. H. Zheng, G. Liu, X. Song, P. Ridgway, S. Xun, and V. S. Battaglia, *J. Electrochem. Soc.*, **157**, A1060 (2010).
25. G. Liu, H. Zheng, X. Song, and V. S. Battaglia, *J. Electrochem. Soc.*, **159**, A214 (2012).
26. H. K. Park, B. S. Kong, and E.-S. Oh, *Electrochem. Commun.*, **13**, 1051 (2011).
27. Z. H. Chen, L. Christensen, and J. R. Dahn, *J. Appl. Polym. Sci.*, **91**, 2958 (2004).
28. M. Yoo, C. W. Frank, S. Mori, and S. Yamaguchi, *Polym.*, **44**, 4197 (2003).
29. A. Guerfi, M. Kaneko, M. Petitclerc, M. Mori, and K. Zaghib, *J. Power Sources*, **163**, 1047 (2007).
30. P. J. Burnett and D. S. Rickerby, *Thin Solid Films*, **154**, 403 (1987).
31. F. Davanloo, C. Collins, and K. Koivusaari, *J. Mater. Res.*, **14**, 3474 (1999).
32. A. C. Fischer-Cripps, *Introduction to contact mechanics*, Springer Verlag (2000).
33. X. Li, W. Xu, M. A. Sutton, and M. Mello, *Nanotechnology, IEEE Transactions on*, **6**, 4 (2007).
34. Y. Qi and S. J. Harris, *J. Electrochem. Soc.*, **157**, A741 (2010).
35. J. Tan, Y. Chao, J. Van Zee, X. Li, X. Wang, and M. Yang, *Mater. Sci. Eng., A*, **496**, 464 (2008).
36. X. Li, Y. H. An, Y. D. Wu, Y. C. Song, Y. J. Chao, and C. H. Chien, *J. Biomed. Mater. Res-A*, **80**, 25 (2007).
37. M. A. Sutton, C. Mingqi, W. H. Peters, Y. J. Chao, and S. R. McNeill, *Image Vis. Comput.*, **4**, 143 (1986).
38. J. Chong, S. Xun, H. Zheng, X. Song, G. Liu, P. Ridgway, J. Q. Wang, and V. S. Battaglia, *J. Power Sources*, **196**, 7707 (2011).
39. C. Creton, in *Adhesive Joints: Formation, Characteristics and Testing*, Vol. 2, K. L. Mittal, Editor, pp. 49–60, VSP, Utrecht, The Netherlands 2002.
40. W. Porcher, B. Lestriez, S. Jouanneau, and D. Guyomard, *J. Power Sources*, **195**, 2835 (2010).
41. B. J. Briscoe, P. D. Evans, E. Pellilo, and S. K. Sinha, *Wear*, **200**, 137 (1996).